Self-Sealing Metal-Supported SOFC Fabricated by Plasma Spraying and Its Performance under Unbalanced Gas Pressure

Jiu-Tao Gao[1] · Jia-Hong Li[1] · Yue-Peng Wang[1] · Chang-Jiu Li[1] · Cheng-Xin Li[1]

Abstract A novel self-sealing structure for metal-supported solid oxide fuel cells (MS-SOFCs) is designed by applying brazing technology between the metal support and interconnector to solve the sealing problem on the anode side of planar SOFCs. A high-reliability self-sealing effect is thus realized at the anode side of the MS-SOFC. Plasma spraying technology is used to prepare cell functional layers including the anode, cathode, and electrolyte. A single cell is assembled with a 50–60-μm plasma-sprayed Sc_2O_3-stabilized ZrO_2 (ScSZ) electrolyte layer. The gas permeability of the self-sealed MS-SOFC without a cathode layer is 0.42×10^{-17} m^2. The open-circuit voltage of the cell is ~ 1.1 V in the operating temperature range from 550 to 750 °C. The power density of the cell reaches 1109 mW cm^{-2} at 750 °C under standard atmosphere. In addition, the use of a fuel gas pressure that is 20 kPa higher than the cathodic gas pressure results in a significant increase in the power density to 1782 mW cm^{-2} at 750 °C. The novel cell structure and gas tightness of the ScSZ electrolyte prepared by plasma spraying indicates that it can meet the requirements of SOFC applications.

Keywords metal-supported solid oxide fuel cells (MS-SOFCs) · plasma spraying · performance · unbalanced gas pressure

✉ Cheng-Xin Li
licx@mail.xjtu.edu.cn

1   State Key Laboratory for Mechanical Behavior of Materials, School of Materials Science and Engineering, Xi'an Jiaotong University, Xi'an, Shaanxi, China

Introduction

Solid oxide fuel cells (SOFCs) can directly convert chemical energy stored in fuel gas to electrical energy, which offers many advantages such as high efficiency, low emissions, and environmental friendliness (Ref 1-3). The two main challenges in commercialization of SOFC technology are cost and reliability, which can be solved by lowering the operating temperature (Ref 4-6). In recent years, the operating temperatures of SOFCs have been reduced to below 750 °C or even lower, enabling the application of more metallic materials in SOFC systems (Ref 7-9). The component supporting the ceramic functional layers in metal-supported SOFCs (MS-SOFCs) are made of porous metallic material. In comparison with traditional all-ceramic SOFCs, MS-SOFCs offer some advantages such as higher thermal conductivity, electrical conductivity, redox stability, tolerance to redox cycles, and mechanical strength (Ref 6, 10-12). The material cost of MS-SOFC is lower than that of electrolyte- or anode-supported SOFC (Ref 13). In addition, the machinability of the metallic material facilitates MS-SOFC assembly (Ref 14). Meanwhile, due to the high strength of the metallic material, MS-SOFCs can withstand repeated and rapid thermal cycling (Ref 12).

SOFCs require hermetic sealing to separate the fuel and oxidant within the cell. The requirements for a SOFC sealing material are severe, since the cell operates at high temperature for thousands of hours with the sealing material exposed to both oxidizing and reducing conditions (Ref 15, 16). Generally, several types of glass and glass ceramics based on borates, phosphates, and silicates are used for this (Ref 15). Compared with conventional ceramic cells, MS-SOFCs can start faster, thus placing strict demands on the sealing material. Therefore, sealing of MS-

SOFCs is closely linked to taking advantage of their full benefits. MS-SOFCs offer many advantages as mentioned above, but they also suffer from many limitations (Ref 17-19). Due to the different physical and chemical properties of metal and ceramic components, the conventional sintering fabrication process is not fully competent. Sintering of SOFC functional layers requires high temperatures (the electrolyte layer usually above 1200 °C, and electrode layers about 1000 °C) in an oxidizing atmosphere (Ref 20-22). The porous metallic material is oxidized in an oxidizing atmosphere at higher temperature. Although many technologies [e.g., electron beam physical vapor deposition (EB-PVD) (Ref 23) and wet chemical processing (Ref 9, 24)] have been used to solve this problem, it is difficult to avoid oxidation of the porous metal. Plasma spraying technology has already been used to deposit porous anode, cathode, and protective coatings for the metal interconnector (Ref 25-27). A special optimized version of the plasma spraying process enables direct deposition of the electrolyte without post-heat treatment. This fast and economic method of preparing thin ceramic layers has received increasing attention. Many problems caused by high-temperature sintering treatment such as the chemical interaction and metal oxidation can thus be avoided (Ref 4, 28, 29).

In this study, a novel self-sealing structure for MS-SOFCs was designed to resolve the sealing problem of planar SOFCs on the anode side by using brazing technology. The anode, electrolyte, and cathode are directly deposited onto porous metal supports using plasma spraying. The gas permeability of the self-sealing MS-SOFC without a cathode layer is measured. The performance of the MS-SOFCs is analyzed by I–V, I–P, and electrochemical impedance spectroscopy (EIS) curves. Moreover, a high-reliability self-sealing effect at the anode side is realized in the MS-SOFCs. The output performance and thermal cycling stability of the cell are investigated under unbalanced gas pressure condition between the anode and cathode side.

Experimental Procedures

New Structure

Figure 1(a) shows a schematic representation of a self-sealing MS-SOFC. Both the interconnector and porous support (SUS 430) were prepared in our laboratory. The thickness of the porous metal support was about 1 mm, and its diameter was 2.5 cm. First, acetone was used to clean the surface of the interconnector and support, then Ni-based solder (Ni/Cr/Si/Fe/B: 83/7/1.5/5.5/3 wt.%) was pasted to the edge of the interconnector. After that, the

support and interconnector were assembled together carefully. Finally, the assembly was placed into a vacuum furnace. Figure 1(b) shows the parameters of the brazing process. In this work, the welding temperature of the Ni-based solder is about 1100 °C, which is much higher than the operating temperature of the MS-SOFC (< 750 °C) (Fig. 2).

Preparation of Functional Layers

The parameters used for preparing the functional layers of the MS-SOFCs are presented in Table 1. Atmospheric plasma spraying (APS) (GDP-80, Jiujiang, 80 kW class) was applied to fabricate the anode layer on the porous metal support. Composite powder (50/50 wt.%) of NiO and GDC (10 mol.%-Gd_2O_3-doped CeO_2) (TERIO CORPORATION, N80898) was used as the anode material with a particle size distribution of 20–50 μm. Fused and crushed ScSZ powder (FUJIMI, 565E5) with particle size distribution of 5–25 μm was used as the electrolyte material. The electrolyte layer was deposited by very-low-pressure plasma spraying (VLPPS) (MF-P 1000 APS/VPS, GTV, Germany). $La_{0.6}Sr_{0.4}Co_{0.2}Fe_{0.8}O_3$ (LSCF) powder (METCO, 6830A) was used as the cathode material with a particle size distribution of 20–70 μm. The LSCF cathode layer was prepared by APS. The area of the cathode was 0.785 cm^2 (diameter 1 cm). Before preparation of the layers, the substrate was preheated by using the plasma. In particular, to prevent overheating during the preparation of the electrolyte layer, an interval of 30 s was allowed between two passes.

Characterization of MS-SOFCs

The gas permeability of the self-sealing cells was measured after preparation of the electrolyte layer was completed. Before measuring the gas permeability, the cells without a cathode layer were reduced in H_2 atmosphere at 750 °C for 2 h. Refer to Ref 30 for more details on the gas permeability testing. The ScSZ electrolyte layer was characterized by X-ray diffraction (XRD) analysis (D/MAX-2400, Rigaku) using Cu K_α radiation. Silver paste was coated on the LSCF cathode for current collection. The open-circuit voltage was measured from 750 to 550 °C during the decline in temperature. EIS of the cell was carried out by using a Solartron SI 1260/1287 impedance analyzer under open-circuit voltage (OCV) condition with a sweeping frequency range of 0.1–10^5 Hz and an alternating circuit (AC) voltage with amplitude of 20 mV. The microstructure of the cell layers was observed by scanning electron microscopy (SEM, VEGA II-XMU, TESCAN, Czech Republic). The output performance of the cell was tested by using a 2440 5A SourceMeter (Keithley, USA) with 50

Fig. 1 (a) Schematic representation of self-sealing MS-SOFCs; (b) Parameters of brazing process
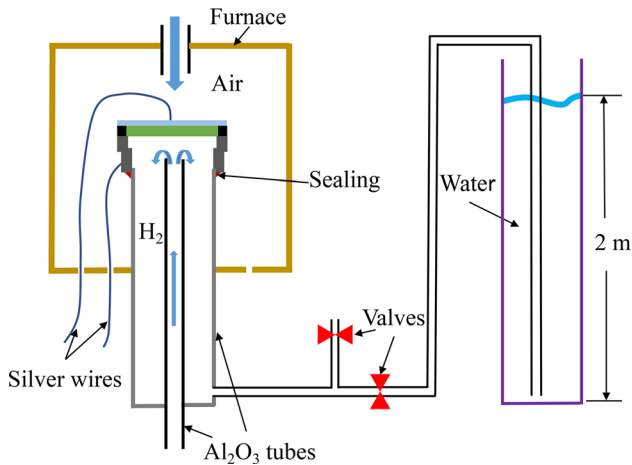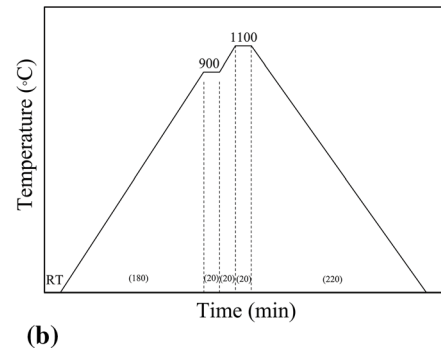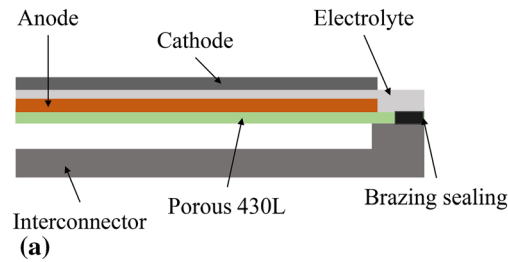

(a)

(b)

Fig. 2 Schematic representation of experimental equipment for cell output performance

sccm humidified hydrogen (3% H_2O) and 200 sccm air under standard and unbalanced (20 kPa) gas pressure conditions, respectively. Five thermal cycles were implemented in 200 h. Each cycle was from 550 to 750 °C then to 550 °C, and the whole heating/cooling cycle lasted for 48 min. Until the next thermal cycle, the operating temperature was kept at 550 °C.

Results and Discussion

Microstructure of Brazed Sealing Area and Gas Permeability of Self-Sealing MS-SOFC

To obtain a good brazing sealing effect, furnace brazing was carried out at 1100 °C for 20 min. The Ni-based solder has good wettability under these brazing conditions, so it is expected to result in good adhesion between the support and interconnector. Figure 3(a) shows the cross-sectional microstructure of the brazed sealing area between the porous metal support and interconnector. The interface between the support and interconnector is bonded well, and the edge of the support is also sealed at the same time, as

shown in Fig. 3(b). The gas permeability of the self-sealing MS-SOFC without a cathode layer was 0.42×10^{-17} m^2, indicating good gas tightness of the brazed cell structure and electrolyte layer.

XRD Pattern and Microstructure of Cell

Figure 4 shows the XRD patterns of the electrolyte layer in different states compared with the pattern for the original powder. Since the cathode area of the cell was smaller than the electrolyte, XRD analysis of the electrolyte layer was performed before (as-sprayed) and after the cell test (after tested). The phase of the original powder was cubic. When the powder was sprayed onto the surface of the anode layers, only one phase was present. After measuring the performance of the MS-SOFC, the ScSZ electrolyte layer was again analyzed by XRD. The result showed that the ScSZ electrolyte layer prepared by VLPPS retained a stable state.

Figure 5(a) shows the typical cross-sectional microstructure of the plasma-sprayed MS-SOFC. The bottom layer is the porous metal support, with a Ni/GDC anode layer (on the top), ScSZ electrolyte layer, and LSCF cathode layer. The thickness of the functional layers is 10–20, 50–60, and 20–30 μm, respectively. Figure 5(b) shows the magnified microstructure of the electrolyte layer prepared by VLPPS. Although some microcracks and voids can still be seen, the interface bonding between lamellae has been greatly improved in comparison with the coating prepared by APS. Defects (e.g., voids, cracks) may appear in ceramic coatings during preparation by plasma spraying (Ref 31, 32). When a splat cools, there is a large temperature gradient between it and the substrate. Some cracks are caused by the quenching stress in the splat. At the same time, the improved interface combination allows the crack to develop in the vertical direction to release the quenching stress (Ref 33). Figure 5(c) and (d) show the interfaces between the anode, cathode, and electrolyte. It can be easily observed that the adhesion between them was good, which is conducive to reduce the contact resistance. In addition, the interface

Table 1 Plasma spraying parameters for preparing functional layers of MS-SOFCs

Parameter	Anode	Electrolyte	Cathode
Method	APS	VLPPS	APS
Powders	NiO/GDC	ScSZ	LSCF
Power (kW)	35	60	30
Current (A)	500	680	500
Gas components (L min^{-1})	Ar/H$_2$ (50/3)	Ar/H$_2$ (60/10)	Ar/H$_2$ (50/1)
Spraying distance (mm)	100	250	100
Torch traverse speed (mm s^{-1})	400	500	400

Fig. 3 Cross-section of brazed sealing area: (a) macromorphology; (b) magnified morphology
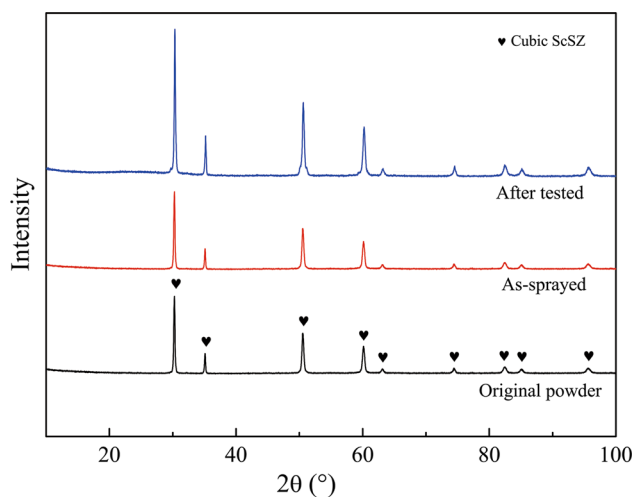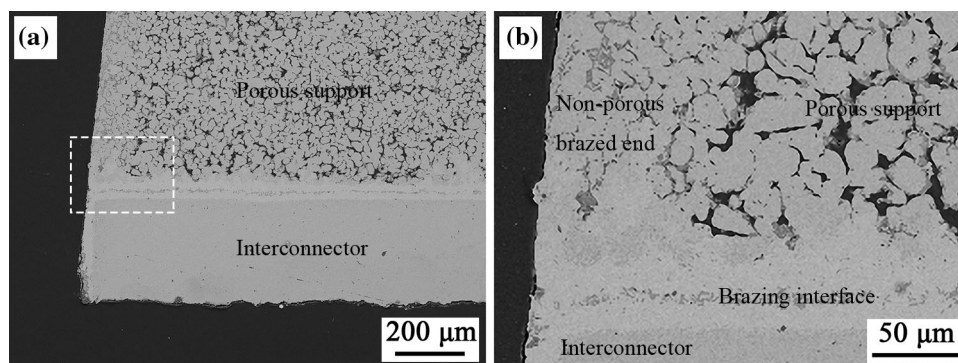
Fig. 4 XRD patterns of ScSZ electrolyte layer in different states

Output Performance

Figure 6(a) shows the output performance curves of the cell at 550, 600, 650, 700, and 750 °C. The open-circuit voltage (OCV) of the self-sealing MS-SOFC was 1.06, 1.06, 1.06, 1.05, and 1.03 V at 550, 600, 650, 700, and 750 °C, respectively. The theoretical voltage of the cell is about 1.1 V at atmospheric pressure with humidified hydrogen (3% H$_2$O) and air as the working gas. These high OCV values reveal that the novel structure of the cell was well sealed and the ScSZ electrolyte prepared by VLPPS was dense enough. Meanwhile, the maximum power density of the cell was 86, 199, 401, 703, and 1109 mW cm^{-2} at 550, 600, 650, 700, and 750 °C, respectively.

Generally, a lamellar and porous microstructure is formed in coatings fabricated by plasma spraying (Ref 13, 18, 34). Due to the open pores in the coating, the OCV and efficiency of cells are generally low. It has been reported that the OCV of SOFCs is about 0.9 V, when the electrolyte layer is directly deposited by APS (Ref 30). To achieve a high level of gas tightness, the thickness of the electrolyte deposited by APS should be no less than 200 μm (Ref 13). In this case, considerable internal resistance is caused by the electrolyte layer because of its low ionic conductivity. Another way to improve the gas-tightness level of the electrolyte has been reported: it was reported that the gas permeability of a YSZ coating decreased to 0.5×10^{-17} m^2 from a value of 5.38×10^{-17} m^2 measured in the as-sprayed state as a result of nitrate infiltration

roughness of the cell fabricated by plasma spraying was significantly large. This is helpful to increase the reaction sites and improve the cell performance. A porous anode can be seen in Fig. 5(c); its porosity is ∼ 25 vol.% due to the reduction of NiO corresponding to Ni (Ref 8). Although the porosity of the cathode is ∼ 15 vol.%, many vertical cracks can be sen in Fig. 5(d), which facilitate oxygen diffusion into three-phase boundary (TPB).

Fig. 5 Cross-section of MS-SOFC after performance testing: (a) complete cell, (b) electrolyte, (c) interface of electrolyte and anode, and (d) interface of electrolyte and cathode
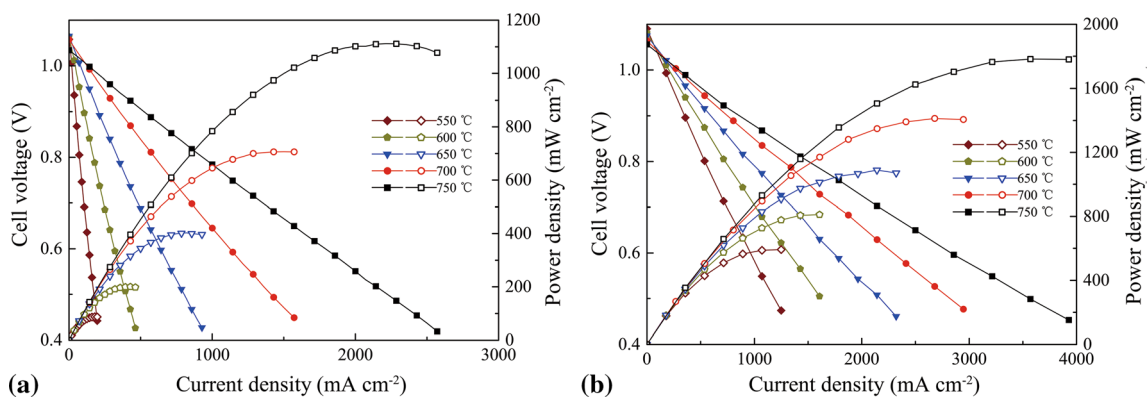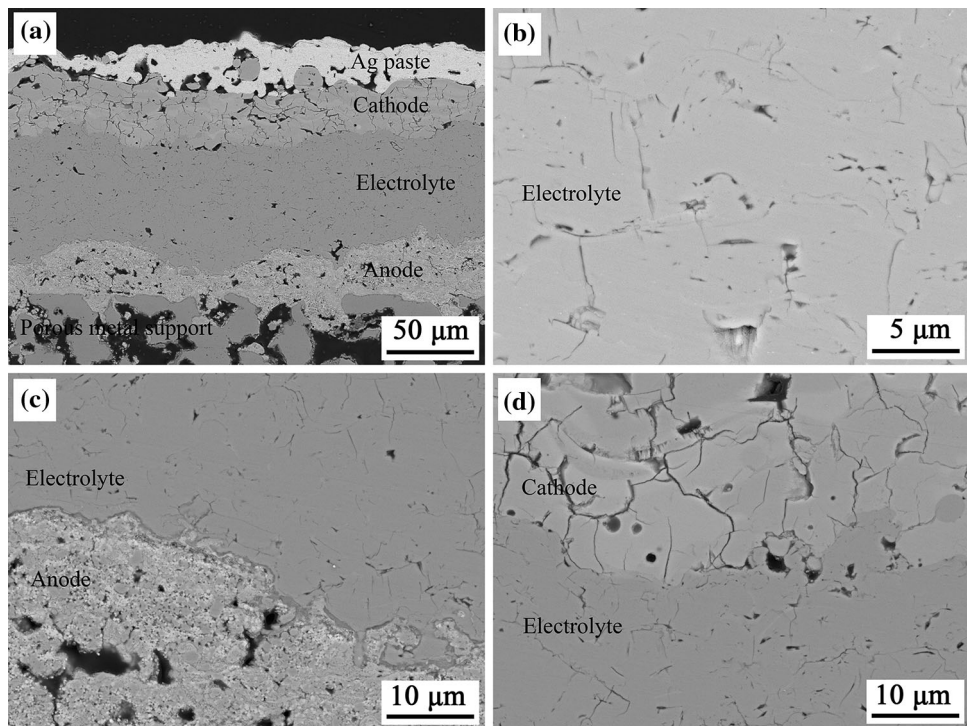

Fig. 6 Output performance of cell at 550, 600, 650, 700 and 750 °C under different testing conditions: (a) standard atmosphere, and (b) 20 kPa

(Ref 30). Application of VLPPS technology is expected to directly prepare thin dense electrolytes. The working pressure of VLPPS is about 100 Pa. Under this condition, the plasma jet is significantly expanded. Not only increasing the spraying distance but also decreasing the interaction between the molten particles and surrounding cold gas result in high speed and temperature of particles before their deposition on the substrate (Ref 35, 36). It has been proved that high speed and temperature of the particles can increase the density of coatings (Ref 31, 37-39). The lamella bonding and the conductivity of the coatings are both improved. There are other reasons which can promote the output performance of the cell. Generally, the porosity obtained in coatings deposited by plasma spraying is 5–15% by volume, which is lower than the ~ 40 vol.%

required for the anode layer (Ref 13). However, the cell still shows good performance, partly because the NiO component can be reduced to Ni, but also because only a ~ 20 μm anode layer is directly deposited on the porous metal support. A number of vertical cracks in the cathode layer ensure smooth diffusion of oxygen. The normal operating temperature of a SOFC is around 800 °C (Ref 2, 40), but it is desired to develop cells that operate at reduced temperatures, as low as 650 °C.

The self-sealing design using brazing can resist a pressure difference between the anode and cathode. To test the sealing reliability under an unbalanced gas pressure condition, a resistance of 20 kPa was applied at the fuel gas outlet. The output performance curves of the cell with higher fuel gas pressure at 550, 600, 650, 700, and 750 °C

Table 2 Maximum power density of several cells prepared by different methods

Cell materials	T, °C	Maximum power density, mW cm^{-2}	Method	Ref.
NiO/GDC‖ScSZ‖LSCF	550	593	Plasma spraying	This work (20 kPa)
	650	1088	Plasma spraying	This work (20 kPa)
NiO/GDC‖LSGM‖LSCF	650	910	Sintering	(Ref 41)
NiO/YSZ‖LSGM‖LSCF	800	710	Plasma spraying	(Ref 33)
NiO/GDC‖ScSZ‖LSCF	550	340	Sintering	(Ref 42)
NiO/ScSZ‖ScSZ‖LSCF/GDC	550	490	Sintering	(Ref 24)
NiO/YSZ‖YSZ‖LSM	800	810	Sintering	(Ref 43)
NiO/YSZ‖YSZ‖LSM	850	530	Sintering	(Ref 44)
NiO/YSZ‖YSZ‖LSFC	817	890	PS-PVD	(Ref 6)
NiO/YSZ‖YSZ‖Au	800	800	EB-PVD	(Ref 45)

are shown in Fig. 6(b). The open-circuit voltage (OCV) was 1.09, 1.08, 1.07, 1.06, and 1.05 V at 550, 600, 650, 700, and 750°C, respectively. The maximum power density of the cell was 592, 812, 1088, 1411, and 1782 mW cm^{-2} at 550, 600, 650, 700, and 750 °C, respectively. Compared with the values under standard atmosphere, the maximum power density showed a significant increase at each operating temperature. In particular, at lower operating temperatures, the percentage increase appeared to be greater. The results of several studies on the output performance of different cells prepared by various methods are summarized in Table 2, revealing the clear advantage offered by the current approach, which is greatly helpful to reduce the operating temperature of SOFCs by the implementation of unbalanced gas pressure.

Generally, a series of reactions which include gas diffusion, surface absorption/dissociation, and charge transfer are involved in the oxidation of fuel gas and reduction of involved oxygen (Ref 46, 47). EIS can be used to analyze these physicochemical reactions and reveal the key factors that affect the entire process. The inductance caused by the instrument or connecting wires is removed in this work. In the EIS Nyquist plot of the SOFC, the intercept in high-frequency impedance spectra is usually attributed to the ohmic resistance of the electrolyte layer. The intercept between high and low frequency gives the electrode polarization resistance (R_p), including the anodic and cathodic contributions. The EIS data for the full cell at 550, 600, 650, 700, and 750 °C under different testing conditions, shown in Fig. 7(a) and (b), provide insight into the factors that control the cell performance. Corresponding equivalent circuit fits (solid lines) are also shown in Fig. 7(a) and (b). Figure 7(c) shows the equivalent circuit model consisting of a resistance element in series with two R–CPE parallel elements. R_s represents the ohmic resistance in the equivalent circuit. This value is subtracted

from the spectra to easily compare results at different temperatures. Generally, the different frequency ranges in EIS represent different electrode processes. R_1 and R_2 are the resistances of the high- and low-frequency processes, whereas CPE1 and CPE2 are the corresponding constant-phase elements. R_p is the sum of R_1 and R_2 (i.e., $R_p = R_1 + R_2$). Fit values for R_s, R_1, and R_2 are listed in Table 3 (standard atmosphere) and Table 4 (20 kPa). As can be seen from Tables 3 and 4, the values of R_s do not change significantly at operating temperatures of 550 to 750 °C with the change in testing conditions. However, the R_p values change significantly during this process. R_p is 2.91, 1.11, 0.53, 0.30, and 0.18 Ω cm^2, respectively, under standard atmosphere condition but 0.32, 0.22, 0.16, 0.12, and 0.11 Ω cm^2, respectively, under higher fuel gas pressure (20 kPa). From Tables 3 and 4, it can be found that the R_p values dramatically decrease with higher fuel gas pressure. Moreover, the output performance is significantly improved. As mentioned above, the thickness of the porous metal support is $\sim$ 1 mm, which is unfavorable for fuel gas transport. By operating the MS-SOFC at a higher fuel gas pressure, the concentration of reactant is increased, thereby improving the kinetics accordingly. It is worth noting that the R_p values of the cell obtained in this work are smaller than those of other reported cells (Table 5), underlining the potential of this method.

Figure 8(a) and (b) show the relationship between the polarization resistance and temperature under standard atmosphere and higher fuel gas pressure, respectively. R_1 is more strongly affected by temperature than R_2 under both testing conditions. This indicates that the processes related to R_1 and R_2 may be linked with electrochemical charge transfer and gas adsorption/diffusion (Ref 48), respectively. The activation energy related to R_p drops from 1.0 to 0.4 eV with a higher fuel gas pressure. The large difference in the values of the activation energy for the cell under

Fig. 7 Nyquist plots of MS-SOFC impedance data at different temperatures under different testing conditions: (a) standard atmosphere and (b) 20 kPa; (c) the equivalent circuit elements used to fit the measured impedance spectra
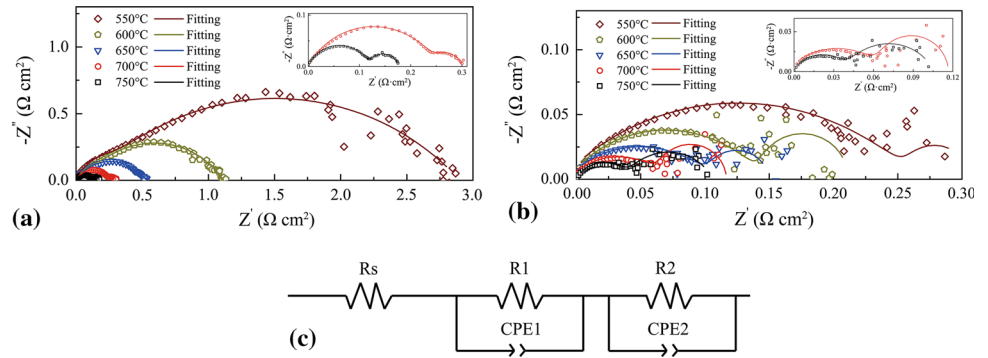

Table 3 Equivalent circuit model fitting results for the EIS data (standard atmosphere)

Temperature, °C	R_s, Ω cm^2	R_1, Ω cm^2	CPE-Q, S s^n cm^{-2}	CPE-n	R_2, Ω cm^2	CPE-Q, S s^n cm^{-2}	CPE-n	R_p, Ω cm^2
550	1.32	2.78	0.024	0.5	0.13	4.05	0.95	2.91
600	0.68	1.04	0.023	0.6	0.07	7.35	1	1.11
650	0.40	0.52	0.028	0.6	0.01	11.73	1	0.53
700	0.27	0.25	0.027	0.7	0.05	3.51	0.87	0.30
750	0.19	0.12	0.029	0.7	0.06	3.8	0.85	0.18

Table 4 Equivalent circuit model fitting results for the EIS data (20 kPa)

Temperature, °C	R_s, Ω cm^2	R_1, Ω cm^2	CPE-Q, S s^n cm^{-2}	CPE-n	R_2, Ω cm^2	CPE-Q, S s^n cm^{-2}	CPE-n	R_p, Ω cm^2
550	1.31	0.28	0.088	0.51	0.04	25.64	1	0.32
600	0.67	0.15	0.072	0.58	0.07	6.246	1	0.22
650	0.38	0.11	0.161	0.52	0.05	10.25	0.93	0.16
700	0.29	0.07	0.200	0.55	0.05	2.346	1	0.12
750	0.16	0.04	0.099	0.69	0.07	4.14	0.70	0.11

**Table 5** Electrode polarization resistance of several cells prepared by different methods

Cell materials	T, °C	R_p, Ω cm^2	Method	Ref.
NiO/GDC‖ScSZ‖LSCF	550	0.32	Plasma spraying	This work (20 kPa)
	650	0.16	Plasma spraying	This work (20 kPa)
NiO/GDC‖LSGM‖LSCF	650	0.66	Sintering	(Ref 41)
NiO/YSZ‖LSGM‖LSCF	800	0.31	Plasma spraying	(Ref 33)
NiO/GDC‖ScSZ‖LSCF	550	0.45	Sintering	(Ref 24)
NiO/YSZ‖YSZ‖LSM	800	0.32	Sintering	(Ref 43)
NiO/YSZ‖YSZ‖LSM	850	0.13	Sintering	(Ref 44)

different testing conditions suggests that, by applying a higher fuel gas pressure, more catalytic sites become accessible (Ref 49).

As mentioned above, the additional pressure implemented at the anode side causes the power density of the cell to increase and R_p to decrease. At the same time, the lower the operating temperature, the more obvious this phenomenon becomes. When the current density is low, activation polarization is obvious. The principle of activated polarization is that all chemical reactions have an energy barrier. The reactants must acquire a certain amount of activation energy to cross this energy barrier for the reaction to proceed smoothly. This energy barrier is the chemical energy. In this work, under standard atmosphere,

Fig. 8 Arrhenius plots of polarization resistance from fitting results for MS-SOFCs under different testing conditions: (a) standard atmosphere and (b) 20 kPa
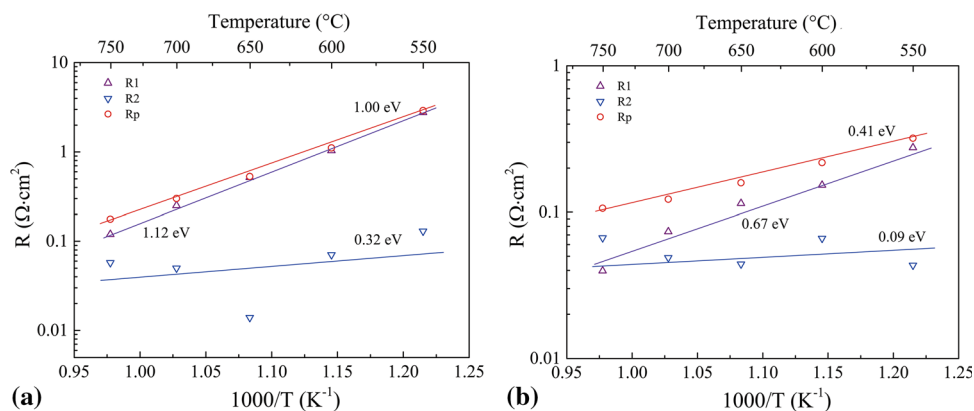
the activation energy was about 1.0 eV, but when an additional pressure of 20 kPa was applied on the anode side, the activation energy was reduced to 0.4 eV.

The anode and cathode activation polarization voltage and current densities can be described by the Butler–Volmer equation (Ref 50):

$$I = I_0 \left[\exp\left(\alpha_a \frac{F}{RT_s} \eta^{act} \right) - \exp\left(\alpha_c \frac{F}{RT_s} \eta^{act} \right) \right], \quad \text{(Eq 1)}$$

where I_0 is the exchange current density, α_a and α_c are the anode and cathode symmetry factors (which are below 1), η^{act} is the activation potential, R is the ideal gas constant, and F is the Faraday constant. Among the parameters in the Butler–Volmer equation, the exchange current density is a very important parameter that can significantly affect the behavior of the activation polarization at the anode. Many models have been proposed to describe exchange current densities. This work considers the model proposed by Yamamura et al. (Ref 51), because it shows an apparent reaction order close to the stoichiometry of the electrochemical reaction at the anode. The following is the equation for the exchange current density I_0:

$$I_{0,anode} = \gamma_{anode} \left(\frac{P_{H_2}}{P_{ref}} \right) \left(\frac{P_{H_2O}}{P_{ref}} \right)^{-0.5} \exp\left(-\frac{E_{act,anode}}{RT_s} \right),$$
$$\text{(Eq 2)}$$

where $I_{0,anode}$ is the exchange current density, γ_{anode} is the preexponential factor, $E_{act,anode}$ is the activation energy of the anode, T_s is the anode temperature, and P_{ref} is the reference pressure. According to literature, the values of γ_{anode} and $E_{act,anode}$ are close to 5.7×10^3 A cm^{-2} and 1.45 eV, respectively. As the anode pressure increases, the anode exchange current density increases, leading to the improvement of the current density. The addition fuel gas pressure (i.e., 20 kPa) at the anode side leads to an increase in the H_2 partial pressure from 97 to 116.4 kPa. In this case, the power density can be increased by only 15% by increasing the anode exchange current density with all other factors held constant. However, when the activation
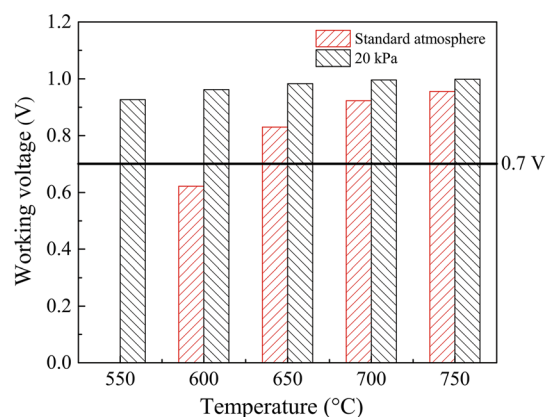

Fig. 9 Working voltage of cell at current density of 300 mA cm^{-2}

energy falls from 1 to 0.41 eV, $I_{0,anode}$ increases by 210 and 55% at 550 and 750 °C, respectively. This therefore suggests that the decrease of the activation energy caused by the 20 kPa extra pressure at the anode side may be the main effect improving the performance of the cell.

Efficiency and Stability

The actual efficiency of the fuel cell is always less than the reversible thermodynamic efficiency. The two major reasons for this are loss of voltage and fuel utilization. The current density of a typical SOFC stack does not exceed 300 mA cm^{-2}, and the working voltage of a single cell is not less than 0.7 V, which are the most important reasons when considering the efficiency (Ref 52). Smaller current density and higher working voltage result in higher efficiency. Figure 9 shows the working voltage of the cell under different testing conditions when the current density is 300 mA cm^{-2}. The working voltage of the cell with the higher fuel gas pressure are all above 0.9 V at 550–750 °C. This indicates that the self-sealing MS-SOFC prepared by plasma spraying is highly efficient and promising for operation below 600 °C. Figure 10 shows the thermal cycling stability of the cell under unbalanced gas pressure.
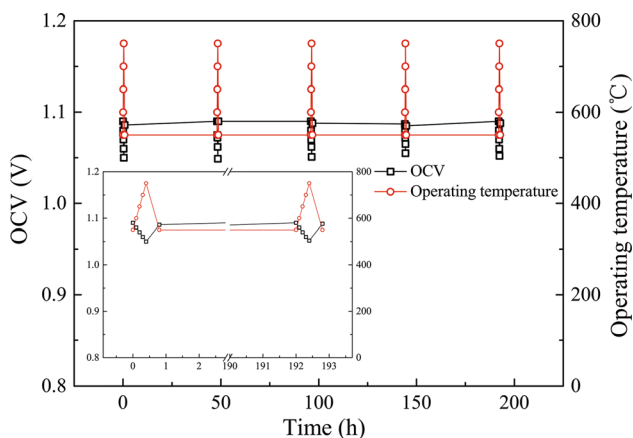
Fig. 10 Thermal cycling stability of cell under unbalanced gas pressure

The OCV was measured as the temperature increased in each thermal cycle. During the course of operation, the OCV of the cell remained stable ($\sim$ 1.06 V). This indicates that the brazed self-sealing cell structure was robust and that the MS-SOFCs prepared by plasma spraying showed good stability.

Conclusions

Self-sealing MS-SOFCs have been designed and deposited by plasma spraying. An electrolyte with thickness of about 50–60 μm was deposited by VLPPS. The OCV of the cell was 1.06, 1.06, 1.06, 1.05, and 1.03 V at 550, 600, 650, 700, and 750°C, respectively, with corresponding maximum power density of 86, 199, 401, 703, and 1109 mW cm^{-2}. When the fuel gas pressure was higher (i.e., by 20 kPa) than the cathodic gas pressure, the maximum power density increased to 1782 mW cm^{-2} at 750 °C. Compared with the values obtained under standard atmosphere, the polarization resistance and maximum power density both changed greatly under higher fuel gas pressure. The activation energy of the polarization resistance of the cell dropped from 1.0 to 0.4 eV. When the current density was 300 mA cm^{-2}, the working voltage of the cell with higher fuel gas pressure was above 0.9 V at 550–750 °C. This indicates that the self-sealing MS-SOFC prepared by plasma spraying was highly efficient and is promising for operation below 600 °C. The results of thermal cycling tests demonstrated the good stability of the self-sealing MS-SOFC prepared using this method.

References

1. M. van den Bossche and S. McIntosh, in *Direct Hydrocarbon Solid Oxide Fuel Cells, Fuel Cells: Selected Entries from the Encyclopedia of Sustainability Science and Technology*, ed. by K.-D. Kreuer (Springer, New York, 2013), p. 31-76
2. S.P.S. Badwal, S. Giddey, A. Kulkarni, J. Goel, and S. Basu, Direct Ethanol Fuel Cells for Transport and Stationary Applications—A Comprehensive Review, *Appl. Energy*, 2015, **145**, p 80-103
3. A.A. Ahmad, N.A. Zawawi, F.H. Kasim, A. Inayat, and A. Khasri, Assessing the Gasification Performance of Biomass: A Review on Biomass Gasification Process Conditions, Optimization and Economic Evaluation, *Renew. Sustain. Energy Rev.*, 2016, **53**, p 1333-1347
4. N. Laosiripojana, W. Wiyaratn, W. Kiatkittipong, A. Arpornwichanop, A. Soottitantawat, and S. Assabumrungrat, Reviews on Solid Oxide Fuel Cell Technology, *Eng. J.*, 2009, **13**(1), p 65-84
5. J. Patakangas, Y. Ma, Y. Jing, and P. Lund, Review and Analysis of Characterization Methods and Ionic Conductivities for Low-Temperature Solid Oxide Fuel Cells (LT-SOFC), *J. Power Sources*, 2014, **263**, p 315-331
6. D. Marcano, G. Mauer, R. Vaßen, and A. Weber, Manufacturing of High Performance Solid Oxide Fuel Cells (SOFCs) with Atmospheric Plasma Spraying (APS) and Plasma Spray-Physical Vapor Deposition (PS-PVD), *Surf. Coat. Technol.*, 2017, **318**, p 170-177
7. C.-S. Hwang, C.-H. Tsai, J.-F. Yu, C.-L. Chang, J.-M. Lin, Y.-H. Shiu, and S.-W. Cheng, High Performance Metal-Supported Intermediate Temperature Solid Oxide Fuel Cells Fabricated by Atmospheric Plasma Spraying, *J. Power Sources*, 2011, **196**(4), p 1932-1939
8. B. Shri Prakash, S. Senthil Kumar, and S.T. Aruna, Properties and Development of Ni/YSZ as an Anode Material in Solid Oxide Fuel Cell: A Review, *Renew. Sustain. Energy Rev.*, 2014, **36**, p 149-179
9. V.V. Krishnan, Recent Developments in Metal-Supported Solid Oxide Fuel Cells, *Wiley Interdiscip. Rev. Energy Environ.*, 2017, **6**(5), p e246
10. Y. Zhou, X. Xin, J. Li, X. Ye, C. Xia, S. Wang, and Z. Zhan, Performance and Degradation of Metal-Supported Solid Oxide Fuel Cells with Impregnated Electrodes, *Int. J. Hydrog. Energy*, 2014, **39**(5), p 2279-2285
11. S.F. Yang, C.S. Hwang, C.H. Tsai, C.L. Chang, and M.H. Wu, Production of Metal-Supported Solid Oxide Fuel Cell Using Thermal Plasma Spraying Technique, *IEEE Trans. Plasma Sci.*, 2017, **45**, p 318-322
12. F. Thaler, D. Udomsilp, W. Schafbauer, C. Bischof, Y. Fukuyama, Y. Miura, M. Kawabuchi, S. Taniguchi, S. Takemiya, A. Nenning, A.K. Opitz, and M. Bram, Redox Stability of Metal-Supported Fuel Cells with Nickel/Gadolinium-Doped Ceria Anode, *J. Power Sources*, 2019, **434**, p 226751
13. R. Hui, Z. Wang, O. Kesler, L. Rose, J. Jankovic, S. Yick, R. Maric, and D. Ghosh, Thermal Plasma Spraying for SOFCs: Applications, Potential Advantages, and Challenges, *J. Power Sources*, 2007, **170**(2), p 308-323
14. M.C. Tucker, Development of High Power Density Metal-Supported Solid Oxide Fuel Cells, *Energy Technol.*, 2017, **5**(12), p 2175-2181

15. P.K. Ojha, T.K. Chongdar, N.M. Gokhale, and A.R. Kulkarni, Investigation of Crystallization Kinetic of SrO-La$_2$O$_3$-Al$_2$O$_3$-B$_2$O$_3$-SiO$_2$ Glass and Its Suitability for SOFC Sealant, *Int. J. Hydrog. Energy*, 2011, **36**(22), p 14996-15001

16. B. Cela Greven, S. Gross-Barsnick, T. Koppitz, R. Conradt, F. Smeacetto, A. Ventrella, and M. Ferraris, Torsional Shear Strength of Novel Glass-Ceramic Composite Sealants for Solid Oxide Fuel Cell Stacks, *Int. J. Appl. Ceram. Technol.*, 2018, **15**(2), p 286-295

17. R. Henne, Solid Oxide Fuel Cells: A Challenge for Plasma Deposition Processes, *J. Therm. Spray Technol.*, 2007, **16**(3), p 381-403

18. R. Vaßen, D. Hathiramani, J. Mertens, V.A.C. Haanappel, and I.C. Vinke, Manufacturing of High Performance Solid Oxide Fuel Cells (SOFCs) with Atmospheric Plasma Spraying (APS), *Surf. Coat. Technol.*, 2007, **202**(3), p 499-508

19. M. Marr, J. Kuhn, C. Metcalfe, J. Harris, and O. Kesler, Electrochemical Performance of Solid Oxide Fuel Cells Having Electrolytes Made by Suspension and Solution Precursor Plasma Spraying, *J. Power Sources*, 2014, **245**(1), p 398-405

20. A. Kumar, A. Jaiswal, M. Sanbui, and S. Omar, Scandia Stabilized Zirconia-Ceria Solid Electrolyte (xSc1CeSZ, 5 < x<11) for IT-SOFCs: Structure and Conductivity Studies, *Scripta Mater.*, 2016, **121**, p 10-13

21. R.R. Monteiro and A.C.S. Sabioni, Preparation of Mullite Whiskers Derived from Topaz Doped with Rare Earth Oxides for Applications in Composite Materials, *Ceram. Int.*, 2016, **42**(1), p 49-55

22. E. Yildiz, S. Yilmaz, and O. Turkoglu, The Production and Characterization of Ytterbium-Stabilized Zirconia Films for SOFC Applications, *Int. J. Appl. Ceram. Technol.*, 2016, **13**(1), p 100-107

23. V. Miguel-Pérez, A. Martínez-Amesti, M.L. Nó, J. Calvo-Angós, and M.I. Arriortua, EB-PVD Deposition of Spinel Coatings on Metallic Materials and Silicon Wafers, *Int. J. Hydrog. Energy*, 2014, **39**(28), p 15735-15745

24. G.Y. Cho, Y.H. Lee, S.W. Hong, J. Bae, J. An, Y.B. Kim, and S.W. Cha, High-Performance Thin Film Solid Oxide Fuel Cells with Scandia-Stabilized Zirconia (ScSZ) Thin Film Electrolyte, *Int. J. Hydrog. Energy*, 2015, **40**(45), p 15704-15708

25. M. Mirzaei, A. Simchi, M.A. Faghihi-Sani, and A. Yazdanyar, Electrophoretic Deposition and Sintering of a Nanostructured Manganese–Cobalt Spinel Coating for Solid Oxide Fuel Cell Interconnects, *Ceram. Int.*, 2016, **42**(6), p 6648-6656

26. C. Lamuta, G. Di Girolamo, and L. Pagnotta, Microstructural, Mechanical and Tribological Properties of Nanostructured YSZ Coatings Produced with Different APS Process Parameters, *Ceram. Int.*, 2015, **41**(7), p 8904-8914

27. A. Vardelle, C. Moreau, J. Akedo, H. Ashrafizadeh, C.C. Berndt, J.O. Berghaus, M. Boulos, J. Brogan, A.C. Bourtsalas, A. Dolatabadi, M. Dorfman, T.J. Eden, P. Fauchais, G. Fisher, F. Gaertner, M. Gindrat, R. Henne, M. Hyland, E. Irissou, E.H. Jordan, K.A. Khor, A. Killinger, Y.-C. Lau, C.-J. Li, L. Li, J. Longtin, N. Markocsan, P.J. Masset, J. Matejicek, G. Mauer, A. McDonald, J. Mostaghimi, S. Sampath, G. Schiller, K. Shinoda, M.F. Smith, A.A. Syed, N.J. Themelis, F.-L. Toma, J.P. Trelles, R. Vassen, and P. Vuoristo, The 2016 Thermal Spray Roadmap, *J. Therm. Spray Technol.*, 2016, **25**(8), p 1376-1440

28. M.C. Tucker, Progress in Metal-Supported Solid Oxide Fuel Cells: A Review, *J. Power Sources*, 2010, **195**(15), p 4570-4582

29. P. Fauchais, A. Vardelle, and B. Dussoubs, Quo Vadis Thermal Spraying?, *J. Therm. Spray Technol.*, 2001, **10**(1), p 44-66

30. C.-J. Li, X.-J. Ning, and C.-X. Li, Effect of Densification Processes on the Properties of Plasma-Sprayed YSZ Electrolyte Coatings for Solid Oxide Fuel Cells, *Surf. Coat. Technol.*, 2005, **190**(1), p 60-64

31. M. Friis, C. Persson, and J. Wigren, Influence of Particle in-Flight Characteristics on the Microstructure of Atmospheric Plasma Sprayed Yttria Stabilized ZrO$_2$, *Surf. Coat. Technol.*, 2001, **141**(2–3), p 115-127

32. C.-J. Li, G.-J. Yang, and C.-X. Li, Development of Particle Interface Bonding in Thermal Spray Coatings: A Review, *J. Therm. Spray Technol.*, 2012, **22**(2–3), p 192-206

33. S.-L. Zhang, T. Liu, C.-J. Li, S.-W. Yao, C.-X. Li, G.-J. Yang, and M. Liu, Atmospheric Plasma-Sprayed La0.8Sr0.2-Ga0.8Mg0.2O3 Electrolyte Membranes for Intermediate-Temperature Solid Oxide Fuel Cells, *J. Mater. Chem. A*, 2015, **3**(14), p 7535-7553

34. C. Zhang, W.Y. Li, M.P. Planche, C.X. Li, H. Liao, C.J. Li, and C. Coddet, Study on Gas Permeation Behaviour Through Atmospheric Plasma-Sprayed Yttria Stabilized Zirconia Coating, *Surf. Coat. Technol.*, 2008, **202**(20), p 5055-5061

35. C. Li, H. Guo, L. Gao, L. Wei, S. Gong, and H. Xu, Microstructures of Yttria-Stabilized Zirconia Coatings by Plasma Spray-Physical Vapor Deposition, *J. Therm. Spray Technol.*, 2014, **24**(3), p 534-541

36. Q.-Y. Chen, X.-Z. Peng, G.-J. Yang, C.-X. Li, and C.-J. Li, Characterization of Plasma Jet in Plasma Spray-Physical Vapor Deposition of YSZ Using a < 80 kW Shrouded Torch Based on Optical Emission Spectroscopy, *J. Therm. Spray Technol.*, 2015, **24**(6), p 1038-1045

37. C. Li, C. Li, H. Long, Y. Xing, X. Ning, C. Zhang, H. Liao, and C. Coddet, Characterization of Atmospheric Plasma-Sprayed Sc$_2$O$_3$-ZrO$_2$ Electrolyte Coating, *Solid State Ion.*, 2006, **177**(19–25), p 2149-2153

38. E.-J. Yang, C.-J. Li, G.-J. Yang, C.-X. Li, and M. Takahashi, Effect of Intersplat Interface Bonding on the Microstructure Of Plasma-Sprayed Al$_2$O$_3$ Coating, *IOP Conf. Ser. Mater. Sci. Eng.*, 2014, **61**, p 012022

39. S.-W. Yao, C.-J. Li, J.-J. Tian, G.-J. Yang, and C.-X. Li, Conditions and Mechanisms for the Bonding of a Molten Ceramic Droplet to a Substrate after High-Speed Impact, *Acta Mater.*, 2016, **119**, p 9-25

40. A.J. Jacobson, Materials for Solid Oxide Fuel Cells, *Chem. Mater.*, 2010, **22**(3), p 660-674

41. H. Sun, Y. Chen, F. Chen, Y. Zhang, and M. Liu, High-Performance Solid Oxide Fuel Cells Based on a Thin La0.8Sr0.2-Ga0.8Mg0.2O3-δ Electrolyte Membrane Supported by a Nickel-Based Anode of Unique Architecture, *J. Power Sources*, 2016, **301**, p 199-203

42. Y. Liu, S.-I. Hashimoto, H. Nishino, M. Mori, Y. Funahashi, Y. Fijishiro, A. Hirano, N. Imanishi, and Y. Takeda, Development of Micro-Tubular SOFCs with an Improved Performance via Nano-Ag Impregnation for Intermediate Temperature Operation, *ECS Trans.*, 2007, **7**, p 615

43. Z. Wang, K. Sun, S. Shen, X. Zhou, J. Qiao, and N. Zhang, Effect of Co-sintering Temperature on the Performance of SOFC with YSZ Electrolyte Thin Films Fabricated by Dip-Coating Method, *J. Solid State Electrochem.*, 2010, **14**(4), p 637-642

44. Q. Ma, J. Ma, S. Zhou, R. Yan, J. Gao, and G. Meng, A High-Performance Ammonia-Fueled SOFC Based on a YSZ Thin-Film Electrolyte, *J. Power Sources*, 2007, **164**(1), p 86-89

45. H.Y. Jung, K.-S. Hong, H. Kim, J.-K. Park, J.-W. Son, J. Kim, H.-W. Lee, and J.-H. Lee, Characterization of Thin-Film YSZ Deposited via EB-PVD Technique in Anode-Supported SOFCs, *J. Electrochem. Soc.*, 2006, **153**(6), p A961

46. S.H. Chan and Z.T. Xia, Polarization Effects in Electrolyte/Electrode-Supported Solid Oxide Fuel Cells, *J. Appl. Electrochem.*, 2002, **32**(3), p 339-347

47. D.E. Vladikova, Z.B. Stoynov, A. Barbucci, M. Viviani, P. Carpanese, J.A. Kilner, S.J. Skinner, and R. Rudkin, Impedance

Studies of Cathode/Electrolyte Behaviour in SOFC, *Electrochim. Acta*, 2008, **53**(25), p 7491-7499

48. L. Bian, C. Duan, L. Wang, L. Zhu, R. O'Hayre, and K.-C. Chou, Electrochemical Performance and Stability of La0·5Sr0·5Fe0·9Nb0·1O3- δ Symmetric Electrode for Solid Oxide Fuel Cells, *J. Power Sources*, 2018, **399**, p 398-405

49. K. Ahmed and K. Foger, Kinetics of Internal Steam Reforming of Methane on Ni/YSZ-Based Anodes for Solid Oxide Fuel Cells, *Catal. Today*, 2000, **63**(2), p 479-487

50. P. Costamagna, Modeling of Solid Oxide Heat Exchanger Integrated Stacks and Simulation at High Fuel Utilization, *J. Electrochem. Soc.*, 1998, **145**(11), p 3995

51. S. Sunde, Monte Carlo Simulations of Polarization Resistance of Composite Electrodes for Solid Oxide Fuel Cells, *J. Electrochem. Soc.*, 1996, **143**(6), p 1930

52. N.Q. Minh, Solid Oxide Fuel Cell Technology—Features and Applications, *Solid State Ion.*, 2004, **174**(1), p 271-277